Inkjet printing of a thermolabile model drug onto FDM-printed substrates:

formulation and evaluation

Georgios K. Eleftheriadis,[a] Christos S. Katsiotis,[a] Dimitrios A. Andreadis,[b] Dimitrios Tzetzis,[c] Christos Ritzoulis,[d] Nikolaos Bouropoulos,[e,f] Dimitra Kanellopoulou,[f] Eleftherios G. Andriotis,[a] John Tsibouklis,[g] Dimitrios G. Fatouros.[a*]

[a]Department of Pharmacy, Aristotle University of Thessaloniki, 54124 Thessaloniki, Greece

[b]Department of Oral Medicine/Pathology, School of Dentistry, Aristotle University of Thessaloniki, Thessaloniki, Greece

[c]School of Science and Technology, International Hellenic University, 57001 Thermi, Greece

[d]Department of Food Science and Technology, International Hellenic University, Sindos Campus, Thessaloniki GR-57400, Greece

[e]Department of Materials Science, University of Patras, 26504 Rio, Patras, Greece

[f]Foundation for Research and Technology Hellas, Institute of Chemical Engineering and High Temperature Chemical Processes, 26504 Patras, Greece

[g]School of Pharmacy and Biomedical Sciences, University of Portsmouth, White Swan Road, Portsmouth, PO1 2DT, United Kingdom

*Corresponding author: Dr. Dimitrios G. Fatouros

e-mail: dfatouro@pharm.auth.gr

Abstract

Objective: The inkjet printing (IP) and fused deposition modeling (FDM) technologies have emerged in the pharmaceutical field as novel and personalized formulation approaches. Specific manufacturing factors must be considered in each adopted methodology, i.e., the development of suitable substrates for IP and the incorporation of highly thermostable active pharmaceutical compounds (APIs) for FDM. In this study, IP and FDM printing technologies were investigated for the fabrication of hydroxypropyl methylcellulose-based mucoadhesive films for the buccal delivery of a thermolabile model drug. **Significance:** This proof-of-concept approach was expected to provide an alternative formulation methodology for personalized mucoadhesive buccal films. **Methods:** Mucoadhesive substrates were prepared by FDM and were subjected to sequential IP of an ibuprofen-loaded liquid ink. The interactions between these processes and the performance of the films were evaluated by various analytical and spectroscopic techniques, as well as by *in vitro* and *ex vivo* studies. **Results:** The model drug was efficiently deposited by sequential IP passes onto the FDM-printed substrates. Significant variations were revealed on the morphological, physicochemical and mechanical properties of the prepared films, and linked to the number of IP passes. The mechanism of drug release, the mucoadhesion and the permeation of the drug through the buccal epithelium were evaluated, in view of the extent of ink deposition onto the buccal films, as well as the distribution of the API. **Conclusions:** The presented methodology provided a proof-of-concept formulation approach for the development of personalized mucoadhesive films.

Introduction

The individualized approaches to drug delivery are pronounced through determination of the patient-specific physiological factors [1,2]. Key to the widespread adoption of personalized approaches is the development of rapid and versatile formulation technologies, such as those that may be offered by two-dimensional (2D) or three-dimensional (3D) printing [1].

Among the available 2D printing techniques, piezoelectric and thermal inkjet printing (IP) are most commonly investigated; this is because these are fast and flexible and allow for the accurate deposition of ink droplets onto the substrate, which is most commonly prepared via solvent casting [3,4]. The routine applicability of this multistep approach is limited by the need to achieve homogeneity in the utilized mixtures and by the requirement of a time-demanding drying step for the preparation of the substrates [5]. A variety of commercial and tailor-made substrates for inkjet-printed formulations have been investigated by researchers, including icing or sugar sheets [6,7], porous substrates, and potato starch-based materials [8,9].

Fused deposition modeling (FDM), among the 3D printing techniques, has been utilized most extensively in pharmaceutical research [10]. This technology has aided the development of dosage forms that combine more than one active ingredient [11,12], controlled-release devices [13,14], orodispersible films [15,16], and mucoadhesive structures for the buccal administration of therapeutics [17]. Furthermore, the combinatorial performance of FDM printing and piezoelectric IP has been explored for

the development of personalized formulations with unique track-and-trace identifiers in a single-step process [18]. However, the high melting temperatures and melt viscosities of specific polymers often result in high-temperature treatments, and thus renders the FDM technique incompatible with specific APIs [19].

In this study, IP was utilized as an efficient technique to provide dose accuracy and personalization of a model drug, whereas mucoadhesive substrates for buccal delivery were fabricated by the FDM process, according to Figure 1. The FDM technology can provide an easier way to produce substrates for IP with tailor-made morphological properties (e.g., dimensions, shape), which have been reported to affect patient acceptability of oral 3D-printed films [20], as well as with specific functional characteristics (e.g., mucoadhesion), in contrast to the commercially available substrates. Moreover, FDM provides a competent alternative to the conventional manufacturing techniques for substrates (e.g., solvent casting and injection molding), by avoiding time-demanding steps (e.g., drying) and the need for incorporating additional equipment (e.g., molds). The current approach is built on the general hybridization concept for additive manufacturing of drug delivery systems [21,22]. It has been claimed that the administration of drugs via the oral cavity may provide a dependable and useful alternative to the peroral route, as the formulation avoids the environmental challenges imposed by the segments of the gastrointestinal tract and circumvents the first-pass effect [23]. To achieve the high retention time required for buccal administration, a frequently used mucoadhesive polymer (hydroxypropyl methylcellulose, HPMC) was selected as core material [24]. IBU was selected as model drug, which exhibited thermosensitivity to the specific processing conditions of HPMC via FDM. The drug delivery systems that resulted from this proof-of-concept-approach were evaluated by analytical and spectroscopic techniques, to explore the post-IP

99   alterations induced on the structural/chemical properties of the FDM-printed substrates,

100   as well as by *in vitro* and *ex vivo* studies to determine the performance of the films for

101   buccal applications.

102

103   **Materials and Methods**

104   *Materials*

105   HPMC (Affinisol™ HPMC HME 15LV) was supplied by the Dow Chemical Company

106   (Midland, MI, USA). Propylene glycol (PG, ≥99.5%), polyethylene glycol 400 (PEG),

107   and ethanol (EtOH, ≥98%) were sourced from Sigma–Aldrich (Steinheim, Germany).

108   IBU was obtained from Fagron Hellas (Athens, Greece). All other materials were

109   analytical grade.

110

111   *Quantification of IBU*

112   Quantification of IBU was performed via high-performance liquid chromatography

113   (HPLC). The mobile phase and chromatographic conditions were adapted from a

114   published report [25]. The HPLC system consisted of an LC-10 AD VP pump, an SIL-

115   20A HT autosampler, and an ultraviolet–visible SPD-10A VP detector (Shimadzu,

116   Kyoto, Japan). A Discovery RP Amide C16 column (15 cm, 4.6 mm, 5 μm) (Sigma–

117   Aldrich, Steinheim, Germany) provided the stationary phase. The mobile phase

118   consisted of a mixture of (A) acetonitrile and (B) 25 mM KH_2PO_4 (pH 3), adjusted with

119   phosphoric acid (55:45, A:B). The system operated at a flow rate of 1.0 mL/min and a

120   detection wavelength of 230 nm. The injection volume was set as 30 and 100 μL for *in*

121   *vitro* and *ex vivo* samples, respectively. Standard samples of IBU were tested over the

122   ranges of 0.5–75.0 and 0.1–10.0 μg/mL for *in vitro* and *ex vivo* experiments,

123   respectively ($R^2 \geq 0.999$). The active compound was detected at approximately 7 min.

Solubility studies

125 Solubility studies were conducted in EtOH, PEG, and PG. A specified amount of each

126 solvent (10 mL) was placed in glass vials. The excess saturation solubility of the drug

127 was indicated by the formation of turbid mixtures, following the addition of pre-

128 weighted IBU portions. The samples were magnetically stirred (100 rpm) for 48 h.

129 Subsequently, 4-mL aliquots were withdrawn and centrifuged at 4000 rcf for 20 min.

130 The supernatants were filtered through 0.45-μm PVDF filters and analyzed via HPLC

131 to determine the solubility of IBU in each solvent.

Viscosity of the ink

135 Binary mixtures of the solvents that exhibited optimal solubility were characterized via

136 kinematic viscosity measurements (ν), using a Micro Ostwald viscometer (SI Analytics,

137 Mainz, Germany). The density (ρ) of each mixture was determined gravimetrically, and

138 the dynamic viscosity (n) was calculated ($n = \nu \times \rho$). The same procedure was

139 employed for determining the rheological behavior of drug-containing inks that were

140 prepared by loading the API into the binary mixture.

Preparation of polymeric filament

143 Filaments of HPMC were produced via hot melt extrusion (HME), using a Filabot

144 Original single-screw extruder (Filabot Inc., Barre, VT, USA). A PEG plasticizing

145 agent (5% w/w) was incorporated into the filament [26]. The extruder was operated at

146 172 °C, equipped with a nozzle of 1.60 mm diameter.

FDM printing

149 The polymeric platforms (P0) were designed in Autocad 2019 (Autodesk Inc., San

150 Rafael, CA, USA) as slabs with a volume of $20 \times 20 \times 0.2$ mm^3. The digital templates

151 were exported in the stereolithography file format (.stl) and loaded in a Makerbot

152 Replicator 2X 3D printer (MakerBot Inc., Brooklyn, NY, USA). The layer height was

153 set as 100 μm, and the slabs were rotated on the z-axis by 45° to improve the printing

154 accuracy of the object [17]. The material extrusion and build platform temperatures

155 were set as 210 °C and 70 °C, respectively. The build cycle was realized at a printing

156 speed of 40 mm/sec and 100% infill.

157

158 ***Drug deposition via IP***

159 Post calculating the viscosity of the candidate inks, an IP performance evaluation was

160 employed to determine the composition of the optimal ink, using a Canon MG2950

161 thermal inkjet printer (Canon Inc., Athens, Greece). Square patterns of 24×24 mm^2

162 were printed on blank A4 paper to set the boundaries of the printing region of each

163 square. The area of the patterns was selected in a manner that enabled homogenous

164 partitioning of the ink across the full area of the 3D-printed slabs. The IP performance

165 was visually assessed, and the ink that presented continuous and homogeneous

166 distribution onto the printed areas, while avoiding the free flow through the nozzle of

167 the cartridge of the printer, was selected as the optimal ink. Subsequently, the substrates

168 were repositioned in the 2D-printed areas and attached to the paper using double

169 adhesive tape. The ink was deposited onto the substrates with 1 (P1), 5 (P5), and 9 (P9)

170 consecutive IP passes, to produce dosage forms with specified IBU loading.

171 The lipophilic fluorescent marker Nile Red (NR) was used as a secondary ink

172 for characterization purposes. To reproduce the rheological behavior of the primary ink,

173 a small amount of IBU (1 mg) was replaced with an equal weight of NR. The IP

174 procedure was reapplied to prepare NR-loaded formulations with 1 (PNR1), 5 (PNR5),

175 and 9 (PNR9) passes.

176

177 *Weight and thickness measurements*

178 The average weight of the P0, P1, P5 and P9 samples (n = 10) was determined

179 gravimetrically. The thickness of the films was recorded using a manual caliper.

180

181 *Drug loading*

182 The formulated films were immersed in glass vials, containing 50 mL of

183 acetonitrile:distilled water at 50:50 (v/v), followed by stirring at 200 rpm. Aliquots (5

184 mL) were withdrawn from the containers after 2 h and centrifuged at 4000 rcf for 30

185 min. The supernatants were filtered through 0.45-μm PVDF filters. The drug loading

186 was determined via HPLC.

187

188 *Swelling and surface pH*

189 The swelling capacity of the prepared formulations was determined gravimetrically.

190 Pre-weighed formulations (w_i) were placed in a petri dish and hydrated with 1 mL of

191 simulated saliva fluid (SSF; sodium chloride 0.8% w/v, potassium phosphate

192 (monobasic) 0.019% w/v, sodium phosphate (dibasic) 0.238% w/v; pH 6.8) [17]. At

193 specified time intervals, the films were withdrawn, gently wiped to remove the excess

194 water amount, and re-weighed (w_h), allowing the determination of the swelling index

195 (SI = (w_h − w_i) × 100)/w_i). The surface pH was determined by hydrating the

196 formulations with distilled water (1 mL) until deformation occurred and by attaching

197 the probe of a pH-meter on the surface of the films.

198

8

Morphological evaluation

The morphological features of the filaments and films were examined using a Celestron Digital Microscope Pro (Celestron, Torrance, CA, USA) and by scanning electron microscopy (SEM) using a Zeiss SUPRA 35VP instrument (Zeiss, Oberkochen, Germany).

Confocal laser scanning microscopy (CLSM)

The deposition of the NR-loaded ink onto the polymeric substrates was visualized via a Zeiss LSM 780 instrument (Zeiss, Oberkochen, Germany). The laser excitation wavelength was set at 543 nm, and the images were analyzed using the ImageJ v.1.52p software.

Thermal analysis

Thermogravimetric analysis (TGA; sample weight of ~10 mg; platinum pan; 30–500 °C; 10 °C/min) was performed using a TA Q500 instrument (TA Instruments, New Castle, DE, USA). For differential scanning calorimetry (DSC) experiments, samples were measured (5–10 mg; perforated aluminum pan; 30–250 °C; 10 °C/min) using a DSC 204 F1 Phoenix instrument (Netzsch, Selb, Germany).

X-ray powder diffraction (XRPD)

XRPD analysis was performed using a D8-Advance instrument (Bruker, Karlsruhe, Germany). The diffractograms (Cu-$K_{\alpha1}$; 40 kV, 40 mA) were recorded over the 2θ range of 5°–50° (step size, 0.02°; scanning speed, 0.35 sec/step).

Fourier transform infrared (FTIR) spectroscopy

The FTIR spectra (750–4500 cm^{-1}, 2-cm^{-1} resolution) of the materials and of the associated drug-delivery platforms were recorded using an IR Prestige-21 instrument (Shimadzu, Kyoto, Japan).

Generalized 2D correlation FTIR (2DCorrFTIR)

2DCorrFTIR spectral analysis was utilized to monitor the dynamic spectral changes of the substrates subjected to the external perturbation, i.e. IP passes [27,28]. Drug loaded specimens with 1–12 IP passes were prepared, to enhance the reliability of the method. The data were analyzed using 2D Shige (Shigeaki Morita, Kwansei-Gakuin University, Japan).

Moving-window 2D correlation spectroscopy

Complemental spectral analysis was accomplished by the MW2D technique, to determine the critical levels of the number of IP passes that induced spectral changes on the surface of the drug loaded specimens. The 2D Shige package was used to analyze the spectral data, through the generation of a 2D map spread of the spectral variables as a function of the perturbation (1–12 IP passes) [29].

Mechanical properties

The nanomechanical integrity of the buccal platforms was assessed using a DUH-211 nanomechanical test instrument (Shimadzu, Kyoto, Japan). Indentation tests facilitated the determination of local variations in the indentation hardness (IH) and elastic modulus (Eit) [30]; a total of 10 indentations, randomly scattered on the surface of each film, were averaged for this purpose. The studies were conducted under cleanroom conditions (50% humidity, 25 °C) using a three-sided pyramidal Berkovich tip indenter

249 (average curvature radius of approximately 100 nm). Because the mechanical

250 properties of the samples are sensitive to viscoelastic deformation, the data were

251 normalized by setting the peak load to 3 sec.

252

253 *Folding endurance (FE)*

254 The buccal films were subjected to manual FE tests by repeatedly folding each

255 formulation along a specified point, until severe surface cracks were observed, i.e.,

256 dissociation of 3D-printed filament strings or layers from the main body of the films,

257 and fragmentation of the films into distinct parts.

258

259 *In vitro* **release studies**

260 The release of IBU from the fabricated formulations (P1, P5, and P9) was monitored in

261 SSF for 120 min; to satisfy the requirement for sink-conditions, the films were fixed in

262 metal cages and properly positioned in double-walled glass vessels, containing 50 mL

263 SSF [17,31]. Aliquots (1 mL) were withdrawn at specific time intervals and replaced

264 with fresh and preheated SSF. After centrifugation at 4500 rcf for 25 min, the

265 supernatants were filtered through 0.45-μm PVDF filters and IBU was quantified using

266 HPLC. The *in vitro* release profiles of the buccal films were compared in view of the

267 difference (f_1) and similarity (f_2) factors. The release mechanism was examined by

268 fitting the data to the Higuchi and the Korsmeyer–Peppas kinetic models. The

269 calculation of f_1 and f_2, as well as the fitting of the data to the kinetic models, was

270 accomplished by the DDSolver add-in [32].

271

272 *Mucoadhesion studies*

273 The mucoadhesive performance of the polymeric formulations was assessed using a

TA-XT texture analyzer (TA Instruments, New Castle, DE, USA). The films were fixed onto the probe with double-adhesive tape. Freshly excised (<2 h) porcine buccal mucosa was supplied by a local abattoir. The buccal mucosa was attached onto polyethylene terephthalate (PET) films with cyanoacrylate glue and was properly mounted on the instrument's platform with double adhesive tape. The mucosa was hydrated with 0.1 mL SSF, and contact with the formulations was established by setting a speed of 0.5 mm/sec and an applied force of 5 N. Contact was maintained for 180 sec and the probe was elevated at a speed of 1 mm/sec. The force-versus-distance profiles of the specimens allowed the determination of the corresponding work of adhesion (W_{ad}) and maximum force of detachment (F_{max}).

Residence time

A cyanoacrylate adhesive was used to fix the buccal mucosa onto the inner sidewall of a double-walled glass vessel (37 °C). Hydrated buccal films (50 μL SSF) were attached onto the porcine mucosa by applying light pressure for 30 sec. The vessel was filled with 100 mL of SSF and stirred at 150 rpm. The time taken for the film to detach was recorded as the residence time.

Ex vivo Permeation and histological studies

Permeation studies of IBU through the buccal epithelium were conducted using Franz diffusion cells (diffusion area of 4.9 cm^2). The receptor compartment was filled with 20 mL of phosphate-buffered saline (PBS, pH 7.4), and the temperature was maintained at 37 °C. The porcine buccal mucosa was fixed, and the buccal films were placed with the inkjet-printed side in contact with the mucosa. The donor compartment was filled with 2 mL of SSF. At specified time intervals, aliquots (1 mL) were withdrawn from

the receptor compartment and immediately replenished with fresh PBS that had been maintained at 37 °C. To quantify the amount of IBU that had penetrated the mucosa, the tissue was cut into pieces, placed in polypropylene tubes containing 50 mL of mobile phase, and sonicated for 45 min prior to separation via centrifugation (4500 rcf, 30 min). The IBU content of the filtered (0.45-μm PVDF filters) supernatant was determined via HPLC. The steady-state mass flux (J_{ss}), apparent permeability coefficient (P_{app}), and lag time were evaluated. J_{ss} was determined from the gradient of the linear fraction of the cumulative mass–time profile, and P_{app} was calculated as $P_{app} = J_{ss}/C_d$, where C_d represents the initial IBU concentration in the donor compartment. The lag time was determined via extrapolation of the linear fraction of the curve to the time axis. Subsequently, the mucosal tissues were treated with formalin, embedded in paraffin, and stained with hematoxylin-eosin prior to visualization via an Olympus CX31 optical microscopy (Olympus, Tokyo, Japan).

Statistical analysis

All data were presented as the mean ± standard deviation (SD). The statistical significance (unpaired Student's t-test) was indicated by $p < 0.05$.

Results and Discussion

Development of the ink

The saturation solubility of IBU in EtOH, PG, and PEG is presented in Table S1. The API was readily soluble in EtOH and PG, with concentrations of 709.5 mg/mL and 402.8 mg/mL, respectively. To optimize the viscosity of the ink system according to the demands of the 2D-printing equipment in use, binary systems comprising EtOH as a primary solvent and PG as a viscosity enhancer [8] were subjected to kinematic

324   viscosity measurements, as shown in Table S2. The reported dynamic viscosities for

325   preventing the free flow of ink or the clogging of the nozzle range from 1 mPa×s to 30

326   mPa×s [33]. For drug-free EtOH:PG binary mixtures ranging from 85:15 to 20:80 (v/v),

327   the kinematic viscosity values were in the range of 1.97–18.31 mm^2/s. The gravimetric

328   determination of the density of each mixture allowed the evaluation of the

329   corresponding dynamic viscosity values, which ranged from 1.63 mPa×s to 16.91

330   mPa×s. Visual assessments indicated that the mixture of EtOH:PG 70:30 (v/v), with a

331   dynamic viscosity of 2.40 mPa×s, allowed continuous IP while avoiding the free flow

332   of ink through the nozzle. In view of the expected increase in viscosity post-loading,

333   binary EtOH:PG mixtures with ratios of up to 85:15 (v/v) were produced with IBU

334   loads of 182.5 mg/mL and 243.0 mg/mL, which exhibited viscosity values of 2.40

335   mPa×s and 2.61 mPa×s, respectively. Subsequently, an IP performance evaluation

336   identified the 182.5-mg/mL IBU load system as the most suitable for use with the

337   available equipment.

338

339   ***Preliminary evaluation of buccal films***

340   The substrates, intended for IP, were fabricated by a sequence of solely two crosswise

341   layers deposited during the built cycle. The operating extrusion temperature of FDM

342   significantly affected the constant flow of the molten polymer throughout the printhead,

343   and consequently the presence of defects was evidenced on the surface of the films

344   (data not shown). Thus, the operating extrusion temperature, that allowed the FDM-

345   processing of thin films with minor defects, was set at 210 °C. The average weight and

346   thickness of the 3D-printed films was 135 ± 5 mg and 226 ± 15 μm, respectively.

347   Minimal alterations to the average weight were recorded for the drug-loaded films due

348   to the post-printing evaporation of EtOH, which comprised the predominant fraction of

the liquid ink. Thus, the increase in weight of the P1, P5 and P9 specimens, compared to P0 (Table 1), was statistically insignificant (p > 0.05). Accordingly, the average thickness of the drug-loaded samples was practically insusceptible to alterations, due to the deposition of the liquid ink.

The drug-loading data (Table 1) revealed a positive correlation between the drug content and the number of 2D-printing passes. Drug loss is caused by the application of shear forces to the substrates and the spreading of the deposited ink [34]. The amount of IBU in formulation P5 was quantified as 1.507 ± 0.071 mg, and that in formulation P1 was 0.391 ± 0.020 mg. The drug-loading ratio of P9 (2.787 ± 0.092 mg) to P1 was approximately 7, indicating the precursive drug loss in the IP process. The surface pH of the formulations was determined as 6.5–6.6, which was consistent with the estimated pH of the saliva in the oral cavity [35].

Furthermore, significant alterations were evidenced between the swelling behavior of the fabricated films, related to the increase of IP passes (p < 0.05). The time-dependent swelling behavior of the IBU-free 3D-printed platforms was mirrored by that of formulations P1 and P5: at 90 s, the SI values were within the narrow range of 189%–207% (Figure 2). P9 was less amenable to rapid hydration, as indicated by the SI of approximately 156% at 120 s. Because IP with EtOH-containing liquid inks induces the partial solubilization of the molecules of HPMC-based substrates [9], the differences in the swelling behavior may be better explained by the rate of diffusion of water molecules into the matrix than by the swelling capacity of the formulation.

Morphological evaluation

Stereoscope and SEM images of the filaments and the printed buccal films are presented in Figure 3. The filament exhibited homogeneous structure with minimal surface

defects (Figure 3A and 3F). Consistent with the die swelling effect, the selected

diameter of the orifice of the extruder (1.60 mm) yielded uniform filaments 1.75 ± 0.03

mm in diameter. However, even in the case of negligible variations in the diameter, the

manual caliper measurements facilitated the constant monitoring of the feedstock and

the adjustment of the diameter in the software of the 3D printer.

The FDM-printed film (Figure 3B and 3G) appeared homogeneous. The surface

morphology was affected by the characteristic build paths throughout the FDM process,

which were imprinted on the surface of the P0 sample. Consistent with the diameter of

the nozzle of the 3D printer (400 μm), adjacent pathways occupied a total width of 859

μm, as shown in Figure 3G. Furthermore, HPMC-related structures that appeared

crystalline were evidenced on the surface of the film. The deposition of IBU-loaded ink

onto the FDM-printed platforms affected the surface morphology, as the distinct

pathways were less visible or not detected (Figure 3C–3E and 3H–3J). In accordance

with previous studies, the deposition of EtOH- and PG-containing liquid ink on the

platforms promoted the partial solubilization of the polymer at the surface of the film

[9] and had a plasticizing effect on the HPMC substrate [36]. The occasionally observed

defects onto the surface of the P1, P5 and P9 specimens were attributed to the sequential

deposition of IBU molecules.

CLSM studies

CLSM allowed the determination of the deposition profile of NR on the substrates.

Representative images and 3D-surface plots of the intensity profile for randomly

selected area of the films are presented in Figure 4. The formation of defects was

evidenced on the surface of the buccal films, associated to the deposition of IBU. Areas

of low intensity, which were observed in all cases, are attributed to the combined effects

of discontinuities in the jetting process, incomplete surface coverage by the ink, and defects and cavities in the buccal platforms.

The image analysis results were consistent with the expected absence of fluorescence for the P0 films. For formulations PNR1, PNR5, and PNR9, the fluorescence intensities were determined as 18.26 ± 10.19, 53.41 ± 20.00, and 69.28 ± 17.93 (a.u.), respectively. The intensity ratios of PNR5 and PNR9 to PNR1 (2.9 and 3.8, respectively) were significantly lower than the corresponding drug-loading ratios. In terms of sample opacity and interference [37], the results corresponded to the external surface, rather than the bulk of the buccal platforms, and consequently indicated the diffusion of NR into the platforms.

Thermal analysis

The TGA thermograms and extrapolated thermal degradation onset temperatures (T_o) are presented in Figure 5A and Table S3, respectively. The drug loaded films P1, P5, and P9 presented weight losses of up to 8%, at temperatures of <200 °C. Moreover, the extended weight losses presented an increasing trend, related to the number of IP-passes. Although the thermal degradation of IBU was characterized by an onset at 167 °C, this active compound has been efficiently incorporated in dosage forms via FDM [38,39]; though, the processing temperature in our study was higher than in previous reports, in view of the composition of the filament and the elimination of defects on the surface of the films. Thus, it was implied that the recorded weight losses of P1, P5, and P9 were attributed to the partial thermal degradation of the superficially deposited API, that occurred at a similar temperature to that of the FDM-linked temperature.

Figure 5B presents the recorded DSC thermograms. The thermogram of IBU exhibited a melting endotherm at approximately 80 °C [25]; The pattern of the HPMC

15LV thermogram complied with previous reports [40] that evidenced the glass transition temperature (T_g) of the polymer at *ca.* 100 °C, whereas an additional endotherm was detected at approximately 165 °C. The DSC profiles of the filaments and formulations were consistent with that of the polymer, indicating that the drug was molecularly dispersed into the polymer matrix or that any crystalline drug was below the detection limit of the instrument.

XRPD studies

The diffractograms of the samples are presented in Figure 5C. The crystalline state of plain IBU was indicated by characteristic peaks over the investigated 2θ range. The broad halo near 19.3° was consistent with the mainly amorphous nature of HPMC. In accordance with the SEM and DSC observations, as well as previous reports, the additional peak at 31.7° indicates some polymer crystallinity [41] or the presence of NaCl in Affinisol™ 15LV [40]. Although the presence of IBU fractions were highlighted by the SEM and CLSM results and correlated with the number of IP passes, the drug-loaded specimens followed the diffraction pattern of HPMC. The absence of IBU-related endotherms in the DSC thermograms of P1, P5 and P9 samples, combined with the typical XRPD detection limit of < 5% (w/w) for crystalline components [42,43], indicated the predominant amorphous state of the IBU structures on the surface of the films [44] or the presence of any drug crystallinity well below the detection limit of the instrument.

FTIR spectroscopy

The FTIR spectrum of raw IBU (Figure 5D) exhibited characteristic bands at 2950, 1710, 1510, and 1250 cm^{-1}, corresponding to C-H, C=O, C-C ring, and C-O/O-H

vibrational modes, respectively [45]. The spectrum of PG was characterized by broad

absorption at approximately 3300 cm^{-1} and bands at 2900 and 1050 cm^{-1}, corresponding

to OH, CH$_2$, and C-OH vibrations, respectively [46]. The PEG spectrum exhibited the

characteristic vibrations of terminal OH (3470 cm^{-1}), C-H (2850 cm^{-1}), and C-O (1100

cm^{-1}) [47]. The spectrum of HPMC exhibited bands at 3480, 2950, 1375, and 1065 cm^{-1}, which are attributed to OH stretching, C-H, OH bending, and C-O, respectively [48].

The spectrum of the filament was consistent with that of HPMC. The characteristic

C=O stretching vibration of IBU (1710 cm^{-1}) was detected in the spectra of the films;

the intensity of this band was proportional to the number of IP passes and reflected the

IBU load. The data were further analyzed using 2DCorrFTIR and MW2D.

2DCorrFTIR and MW2D

Application of the 2DCorrFTIR technique [27] generated the synchronous contour plot,

the auto-peaks, and the asynchronous contour plot (Figure 6A–6C). A brief explanation

is presented in Supplementary Information. In accordance with Noda's rules [27], the

sequence of spectral changes at the surface of the film was correlated with the number

of IP passes, as shown in Table 2. The data indicated that there was a relationship

between the band at 1053 cm^{-1} and the absorptions at 1728 and 3414 cm^{-1} and that the

changes in the vibrations at 1728 and 3414 cm^{-1} were not mutually dependent. The

changes of the band at 1053 cm^{-1}, indicated the sequential deposition of the ink onto

the 3D-printed platforms. Variations in the associated H-bonded absorption of C-OH

groups (3414 cm^{-1}) indicated the incorporation of ink-related hydroxyl species onto the

films, which was evidenced by an augmentation of the signals of the C-OH groups of

HPMC and PEG. As expected, the IBU carbonyl absorption (1728 cm^{-1}) was also

correlated with the ink-deposition process, but neither the synchronous map nor the

asynchronous map was capable of identifying any notable correlation with the changes in the C-OH bands of the system.

Complementary MW2D mapping (Figure 6D) allowed visualization of the peak variations across the perturbation axis. The deposition of ink onto the substrate was detected in the MW2D map as IP pass-number-linked alterations in the band at 1053 cm^{-1} over the monitored number of 12 passes. Consistent with the IBU accumulation at the surface of the film, for IP passes 1–6, negligible variations were observed in the carbonyl absorption of IBU (1728 cm^{-1}), but these variations became notable with the increasing number of IP passes (7–12). Variations in the H-bonded absorption (C-OH, 3414 cm^{-1}), which were observed up to the seventh pass, indicated the PG deposition onto the platform.

The spectral analysis results were consistent with the findings of the SI, SEM, CLSM, and XRPD studies, regarding both the ink deposition and drug distribution into the 3D-printed platforms. The deposition of the liquid ink induced partial solubilization of the superficial HPMC molecules. Most of the IBU molecules diffused into the film over 1–6 IP passes, with a parallel accumulation of PG onto the surface, due to the gradual formation of a film-like barrier. At ≥7 IP passes, surface saturation apparently occurred, suggesting the formation of sequential PG layers or the existence of a mass balance between each newly deposited amount of PG and the PG fractions that diffused into the formulation. Furthermore, a corresponding increase in the IBU content at the surface was observed. Consequently, it is assumed that the overlay of PG at the surface of the platform limited the diffusion of IBU into the polymer matrix, followed by a parallel accumulation of drug molecules on the surface of the films.

Mechanical properties

499 Typical force-versus-depth nanoindentation curves and data related to the mechanical

500 properties of the films are presented in Figure 7 and Table 3, respectively. For all the

501 samples, at a peak force of 10 mN, an increasing creep phenomenon was observed with

502 the increasing number of IP passes. The indentation depths were determined at 4.7–

503 6.8 μm. The lowest indentation depth was observed for the IBU-free film. The profiles

504 revealed an increase in plasticity with the increasing number of IP passes, as

505 exemplified by the pronounced differences in the Eit and IH of specimens P9 and P0.

506 A softening behavior was observed, which is a prerequisite for the development of

507 buccal films [49]. Moreover, the increasing flexibility of the buccal films with the

508 increasing number of IP passes was indicated by FE values of 45 ± 1 and 101 ± 5 for

509 formulations P0 and P9, respectively (Table 3).

510

511 ***In vitro release studies***

512 The release profiles of formulations P1, P5, and P9 (Figure 8) indicated a gradual

513 decrease in the release rate of IBU with the increasing number of IP passes employed

514 during the fabrication process. In the case of P1, a burst release of half the IBU load

515 occurred at the onset of the experiment; >80% of the drug was released within 2.5 min.

516 For formulations P5 and P9, 50% of the IBU content was released within 2.5 and 5 min,

517 respectively, 80% was released at 10 and 15 min, respectively, and approximately 100%

518 was released at 30 and 60 min, respectively.

519   The determination of the difference (f_1) and similarity (f_2) factors allowed the

520 statistical comparison of the release profiles of the drug-loaded buccal films, as shown

521 in Table 4. The statistical factors were determined in the time range 0–30 min to avoid

522 the deduction of biased results, as the three latest points of the release profiles were

523 representative of the ultimate IBU release. The similarities in the release behaviors of

formulations P5 and P9, and the markedly different behavior of formulation P1, were evidenced by the obtained values.

To determine the underlying mechanism of IBU release, data for formulations P1, P5 and P9 were fitted to established kinetics models (Table 5). Formulation P1 exhibited burst release behavior, attributed to the superficial deposition of IBU on the film; thus, none of the kinetic models used in the current study were applicable to the release profile of P1. The formulation P5 was fitted to the Higuchi model (full data range, $R^2 = 0.861$), characteristic of the near-inverse proportionality between the rate of drug release and the square root of time. The kinetics of P5 suggest that the phase transition and the swelling behavior of the HPMC-based platform occurred after the complete release of IBU [50]. The film P9 best fitted the Korsmeyer-Peppas model (data corresponding to < 60% IBU released, $R^2 = 0.907$), whereas the value of the release exponent (n = 0.457) indicated the Fickian diffusion mechanism. This is associated with the formation of a film-like barrier, due to the deposition of increased amounts of the ink on the surface of P9 film, which rendered the controlled release behavior of the buccal formulation.

Mucoadhesion and residence time

Evaluations of W_{ad} and F_{max} allowed the investigation of the effect of the number of IP passes on the mucoadhesion performance of the buccal films. Representative mucoadhesion profiles are presented in Figure 9A. The control substrate (P0) was characterized by W_{ad} and F_{max} values of 7.69 ± 0.96 Nm and 4.24 ± 0.68 N, respectively, due to the mucoadhesive nature of HPMC [24]. A comparison of the inkjet-printed films with the P0 specimen (p < 0.05) revealed that the maximum force of adhesion increased with the number of IP passes: F_{max} was determined as 6.81 ± 0.93, $9.42 \pm$

1.14, and 11.86 ± 1.32 N for P1, P5, and P9, respectively. A similar trend was observed for W_{ad}, which was 9.32 ± 1.48, 21.33 ± 2.45, and 23.52 ± 2.16 N×mm for P1, P5, and P9, respectively. The residence time studies confirmed the capability of all formulations to reside at the buccal site over therapeutically relevant timescales.

It may be argued that the incorporation of the plasticizing component (PG) reduced the barrier to rotation of the polymer chains, thus promoting the mucin-polymer interaction, which is a prerequisite for mucoadhesive behavior [51]. However, the benefits to the mucoadhesive behavior imparted by the plasticizer were counterbalanced by the associated increase in the ease of hydration of the films, which if not limited promotes the disentanglement of the mucin–polymer system [52], as indicated by the statistical insignificance between the performance of P5 and P9 ($p > 0.05$).

Permeation and histological studies

The *ex vivo* permeation performance of formulations P5 and P9 is presented in Figure 9B and Table 6. A comparison of the J_{ss} values of P5 (3.65 ± 0.35 µg cm^{-2} h^{-1}) and P9 (11.50 ± 0.61 µg cm^{-2} h^{-1}) indicated the capability of each formulation to promote the permeation of the active ingredient through biological tissues ($p < 0.05$). Similarly, P_{app} was evaluated as 4.82 ± 0.47 cm h^{-1} for P5 and 8.36 ± 0.78 cm h^{-1} for P9 ($p < 0.05$). Both formulations exhibited lag times of <1 h. Consistent with the permeation-enhancing effect of PG [53], the amount of IBU that was extracted from the buccal tissue at the end of the experiment was quantified as 77.4 ± 8.2 µg for P5 and 166.7 ± 15.6 µg for P9.

Complementary histological studies were conducted on the treated mucosa and indicated normal structures on the P0-treated mucosa (Figure 10A). In contrast, the

presence of the permeation enhancer PG at the surface of the applied formulations effected significant alterations at the epithelial level; these were witnessed as mild desquamation of the superficial layer and vacuolation of the squamous cell layers, as shown in Figure 10B and 10C.

Conclusions

For individualized drug delivery, the IP and FDM techniques were combined in the fast and facile fabrication of a mucoadhesive drug delivery system for the buccal administration of a thermolabile API. Significant variations were revealed on the morphological and mechanical properties of the prepared films. The variations were linked to the number of sequential IP passes of the FDM-printed substrates. The 2DCorrFTIR and MW2D techniques indicated the interactions between the FDM-printed material and the 2D-deposited liquid ink. The mechanism of drug release, the mucoadhesion performance and the permeation of the drug through the buccal epithelium were further explored, in view of the extent of ink deposition onto the buccal films, as well as the distribution of the API. The findings highlighted the potential of the combinatorial utilization of the IP and FDM techniques for the proof-of-concept preparation of personalized buccal films, incorporating thermolabile components. This manufacturing approach will benefit the expansion of the available APIs that can be incorporated in FDM-printed drug delivery systems, as in the case of *in situ* manufacturing of mucoadhesive buccal films at the points of care, independently of the thermal properties of the API. However, the drug loading and the release behavior of the films were simultaneously susceptible to alterations, regarding the number of IP passes. Thus, additional studies are required to further investigate the ultimate relation between these features to the nature of the core material and the incorporated API. This

will provide a useful tool for the prediction of the on-demand performance of the buccal films, according to the patients' needs. Furthermore, supplementary research is needed to support the potential of this hybrid approach toward clinically relevant applications.

Declaration of Interest

The authors report no conflict of interest.

References

[1]   Sandler N, Preis M. Printed Drug-Delivery Systems for Improved Patient Treatment. Trends Pharmacol Sci. 2016;37:1070–1080.

[2]   Breitkreutz J, Boos J. Paediatric and geriatric drug delivery. Expert Opin Drug Deliv. 2007;4:37–45.

[3]   Genina N, Janßen EM, Breitenbach A, et al. Evaluation of different substrates for inkjet printing of rasagiline mesylate. Eur J Pharm Biopharm. 2013;85:1075–1083.

[4]   Montenegro-Nicolini M, Reyes PE, Jara MO, et al. The Effect of Inkjet Printing over Polymeric Films as Potential Buccal Biologics Delivery Systems. AAPS PharmSciTech. 2018;19:3376–3387.

624　　[5]　Buanz ABM, Belaunde CC, Soutari N, et al. Ink-jet printing versus solvent

625　　　　casting to prepare oral films: Effect on mechanical properties and physical

626　　　　stability. Int J Pharm. 2015;494:611–618.

627　　[6]　Raijada D, Genina N, Fors D, et al. A Step Toward Development of Printable

628　　　　Dosage Forms for Poorly Soluble Drugs. J Pharm Sci. 2013;102:3694–3704.

629　　[7]　Eleftheriadis G, Monou P, Bouropoulos N, et al. In Vitro Evaluation of 2D-

630　　　　Printed Edible Films for the Buccal Delivery of Diclofenac Sodium. Materials.

631　　　　2018;11:864.

632　　[8]　Sandler N, Määttänen A, Ihalainen P, et al. Inkjet printing of drug substances and

633　　　　use of porous substrates-towards individualized dosing. J Pharm Sci.

634　　　　2011;100:3386–3395.

635　　[9]　Edinger M, Iftimi L-D, Markl D, et al. Quantification of Inkjet-Printed

636　　　　Pharmaceuticals on Porous Substrates Using Raman Spectroscopy and Near-

637　　　　Infrared Spectroscopy. AAPS PharmSciTech. 2019;20:207.

638　　[10]　Gioumouxouzis CI, Karavasili C, Fatouros DG. Recent advances in

639　　　　pharmaceutical dosage forms and devices using additive manufacturing

640　　　　technologies. Drug Discov Today. 2019;24:636–643.

641　　[11]　Goyanes A, Wang J, Buanz A, et al. 3D Printing of Medicines: Engineering

642　　　　Novel Oral Devices with Unique Design and Drug Release Characteristics. Mol

643　　　　Pharm. 2015;12:4077–4084.

644　　[12]　Pereira BC, Isreb A, Forbes RT, et al. 'Temporary Plasticiser': A novel solution

645　　　　to fabricate 3D printed patient-centred cardiovascular 'Polypill' architectures.

646　　　　Eur J Pharm Biopharm. 2019;135:94–103.

647　　[13]　Maroni A, Melocchi A, Parietti F, et al. 3D printed multi-compartment capsular

648　　　　devices for two-pulse oral drug delivery. J Controlled Release. 2017;268:10–18.

649 [14] Eleftheriadis GK, Katsiotis CS, Bouropoulos N, et al. FDM-printed pH-

650   responsive capsules for the oral delivery of a model macromolecular dye. Pharm

651   Dev Technol. 2020;1–7.

652 [15] Jamróz W, Kurek M, Łyszczarz E, et al. 3D printed orodispersible films with

653   Aripiprazole. Int J Pharm. 2017;533:413–420.

654 [16] Musazzi UM, Selmin F, Ortenzi MA, et al. Personalized orodispersible films by

655   hot melt ram extrusion 3D printing. Int J Pharm. 2018;551:52–59.

656 [17] Eleftheriadis GK, Ritzoulis C, Bouropoulos N, et al. Unidirectional drug release

657   from 3D printed mucoadhesive buccal films using FDM technology: In vitro and

658   ex vivo evaluation. Eur J Pharm Biopharm. 2019;144:180–192.

659 [18] Trenfield SJ, Xian Tan H, Awad A, et al. Track-and-trace: Novel anti-counterfeit

660   measures for 3D printed personalized drug products using smart material inks.

661   Int J Pharm. 2019;567:118443.

662 [19] Wei C, Solanki NG, Vasoya JM, et al. Development of 3D Printed Tablets by

663   Fused Deposition Modeling Using Polyvinyl Alcohol as Polymeric Matrix for

664   Rapid Drug Release. J Pharm Sci. 2020;109:1558–1572.

665 [20] Rautamo M, Kvarnström K, Sivén M, et al. Benefits and Prerequisites Associated

666   with the Adoption of Oral 3D-Printed Medicines for Pediatric Patients: A Focus

667   Group Study among Healthcare Professionals. Pharmaceutics. 2020;12:229.

668 [21] Eleftheriadis GK, Katsiotis CS, Genina N, et al. Manufacturing of hybrid drug

669   delivery systems by utilizing the fused filament fabrication (FFF) technology.

670   Expert Opin Drug Deliv. 2020;1–5. doi: 10.1080/17425247.2020.1776260

671 [22] Eleftheriadis GK, Monou PK, Bouropoulos N, et al. Fabrication of

672   mucoadhesive buccal films for local administration of ketoprofen and lidocaine

673 hydrochloride by combining fused deposition modeling and inkjet printing. J

674 Pharm Sci. 2020; S0022-3549(20)30271-9doi: 10.1016/j.xphs.2020.05.022

675 [23] Brandl M, Bauer-Brandl A. Oromucosal drug delivery: Trends in in-vitro

676 biopharmaceutical assessment of new chemical entities and formulations. Eur J

677 Pharm Sci. 2019;128:112–117.

678 [24] Alopaeus JF, Hellfritzsch M, Gutowski T, et al. Mucoadhesive buccal films

679 based on a graft co-polymer – A mucin-retentive hydrogel scaffold. Eur J Pharm

680 Sci. 2020;142:105142.

681 [25] Eleftheriadis GK, Filippousi M, Tsachouridou V, et al. Evaluation of

682 mesoporous carbon aerogels as carriers of the non-steroidal anti-inflammatory

683 drug ibuprofen. Int J Pharm. 2016;515:262–270.

684 [26] Melocchi A, Parietti F, Maroni A, et al. Hot-melt extruded filaments based on

685 pharmaceutical grade polymers for 3D printing by fused deposition modeling.

686 Int J Pharm. 2016;509:255–263.

687 [27] Noda I, Ozaki Y. Two-dimensional correlation spectroscopy: applications in

688 vibrational and optical spectroscopy. Chichester: Wiley; 2004.

689 [28] Noda I. Techniques of two-dimensional (2D) correlation spectroscopy useful in

690 life science research. Biomed Spectrosc Imaging. 2015;109–127.

691 [29] Morita S, Ozaki Y. Moving-window two-dimensional correlation spectroscopy

692 and perturbation-correlation moving-window two-dimensional correlation

693 spectroscopy. Chemom Intell Lab Syst. 2017;168:114–120.

694 [30] Mansour G, Tzetzis D. Nanomechanical Characterization of Hybrid Multiwall

695 Carbon Nanotube and Fumed Silica Epoxy Nanocomposites. Polym-Plast

696 Technol Eng. 2013;52:1054–1062.

697   [31]   Tang C, Guan Y-X, Yao S-J, et al. Preparation of ibuprofen-loaded chitosan

698   films for oral mucosal drug delivery using supercritical solution impregnation.

699   Int J Pharm. 2014;473:434–441.

700   [32]   Zhang Y, Huo M, Zhou J, et al. DDSolver: An Add-In Program for Modeling

701   and Comparison of Drug Dissolution Profiles. AAPS J. 2010;12:263–271.

702   [33]   Varan C, Wickström H, Sandler N, et al. Inkjet printing of antiviral PCL

703   nanoparticles and anticancer cyclodextrin inclusion complexes on bioadhesive

704   film for cervical administration. Int J Pharm. 2017;531:701–713.

705   [34]   Buanz ABM, Saunders MH, Basit AW, et al. Preparation of Personalized-dose

706   Salbutamol Sulphate Oral Films with Thermal Ink-Jet Printing. Pharm Res.

707   2011;28:2386–2392.

708   [35]   Salamatmiller N, Chittchang M, Johnston T. The use of mucoadhesive polymers

709   in buccal drug delivery. Adv Drug Deliv Rev. 2005;57:1666–1691.

710   [36]   Hardy IJ, Cook WG, Melia CD. Compression and compaction properties of

711   plasticised high molecular weight hydroxypropylmethylcellulose (HPMC) as a

712   hydrophilic matrix carrier. Int J Pharm. 2006;311:26–32.

713   [37]   Pygall SR, Whetstone J, Timmins P, et al. Pharmaceutical applications of

714   confocal laser scanning microscopy: The physical characterisation of

715   pharmaceutical systems. Adv Drug Deliv Rev. 2007;59:1434–1452.

716   [38]   Ehtezazi T, Algellay M, Islam Y, et al. The Application of 3D Printing in the

717   Formulation of Multilayered Fast Dissolving Oral Films. J Pharm Sci.

718   2018;107:1076–1085.

719   [39]   Yang Y, Wang H, Li H, et al. 3D printed tablets with internal scaffold structure

720   using ethyl cellulose to achieve sustained ibuprofen release. Eur J Pharm Sci.

721   2018;115:11–18.

722   [40]   Prasad E, Islam MT, Goodwin DJ, et al. Development of a hot-melt extrusion

723   (HME) process to produce drug loaded Affinisol^{TM} 15LV filaments for fused

724   filament fabrication (FFF) 3D printing. Addit Manuf. 2019;29:100776.

725   [41]   Chonkar AD, Rao JV, Managuli RS, et al. Development of fast dissolving oral

726   films containing lercanidipine HCl nanoparticles in semicrystalline polymeric

727   matrix for enhanced dissolution and ex vivo permeation. Eur J Pharm Biopharm.

728   2016;103:179–191.

729   [42]   Newman JA, Schmitt PD, Toth SJ, et al. Parts per Million Powder X-ray

730   Diffraction. Anal Chem. 2015;87:10950–10955.

731   [43]   Venkatesh GM, Barnett ME, Owusu-Fordjour C, et al. Detection of Low Levels

732   of the Amorphous Phase in Crystalline Pharmaceutical Materials by Thermally

733   Stimulated Current Spectrometry. Pharm Res. 2001;18:98–103.

734   [44]   Wong RSH, Dodou K. Effect of Drug Loading Method and Drug

735   Physicochemical Properties on the Material and Drug Release Properties of Poly

736   (Ethylene Oxide) Hydrogels for Transdermal Delivery. Polymers. 2017;9:286.

737   [45]   Namur J, Wassef M, Pelage JP, et al. Infrared microspectroscopy analysis of

738   Ibuprofen release from drug eluting beads in uterine tissue. J Controlled Release.

739   2009;135:198–202.

740   [46]   Suganthi KS, Anusha N, Rajan KS. Low viscous ZnO–propylene glycol

741   nanofluid: a potential coolant candidate. J Nanoparticle Res. 2013;15:1986.

742   [47]   Chieng B, Ibrahim N, Yunus W, et al. Poly(lactic acid)/Poly(ethylene glycol)

743   Polymer Nanocomposites: Effects of Graphene Nanoplatelets. Polymers.

744   2013;6:93–104.

745   [48]   Mahdavinia GR, Ettehadi S, Amini M, et al. Synthesis and characterization of

746   hydroxypropyl   methylcellulose-g-poly(acrylamide)/LAPONITE®   RD

747   nanocomposites as novel magnetic- and pH-sensitive carriers for controlled drug

748   release. RSC Adv. 2015;5:44516–44523.

749   [49] Khan S, Boateng JS, Mitchell J, et al. Formulation, Characterisation and

750   Stabilisation of Buccal Films for Paediatric Drug Delivery of Omeprazole. AAPS

751   PharmSciTech. 2015;16:800–810.

752   [50] Siepmann J, Peppas NA. Modeling of drug release from delivery systems based

753   on hydroxypropyl methylcellulose (HPMC). Adv Drug Deliv Rev. 2012;64:163–

754   174.

755   [51] Llabot JM, Palma SD, Manzo RH, et al. Design of novel antifungal

756   mucoadhesive films. Int J Pharm. 2007;336:263–268.

757   [52] Kaur G, Singh D, Brar V. Bioadhesive okra polymer based buccal patches as

758   platform for controlled drug delivery. Int J Biol Macromol. 2014;70:408–419.

759   [53] Wu X, Desai K-GH, Mallery SR, et al. Mucoadhesive Fenretinide Patches for

760   Site-Specific Chemoprevention of Oral Cancer: Enhancement of Oral Mucosal

761   Permeation of Fenretinide by Coincorporation of Propylene Glycol and Menthol.

762   Mol Pharm. 2012;9:937–945.

763

764

765   **Table 1.** Dose uniformity and surface pH of the fabricated buccal films.

Formulation	P0	P1	P5	P9
Weight (mg)	135 ± 4	136 ± 6	137 ± 6	139 ± 8
Drug content (μg)	-	391 ± 20	1507 ± 71	2787 ± 92
Surface pH	-	6.61 ± 0.11	6.54 ± 0.09	6.63 ± 0.07

766

767

768 **Table 2.** Interpretation of the 2D correlation contour maps.

ν_1	ν_2	Synchronous/asynchronous	Sequence
1053	1728	+/+	ν_1 before ν_2
1053	3414	+/+	ν_1 before ν_2
1728	3414	Not detected	No correlation

769

770

771 **Table 3.** Nanoindentation performance (Eit and IH) and FE of the FDM-printed plain

772 platform (P0) and buccal films after the deposition of the active compound via IP.

Formulation	Eit [MPa]	IH [MPa]	FE
P0	223.24 ± 28.32	46.64 ± 6.65	45 ± 1
P1	204.23 ± 59.02	41.01 ± 7.88	53 ± 3
P5	169.18 ± 35.42	36.59 ± 7.58	90 ± 2
P9	140.50 ± 42.49	24.69 ± 7.37	101 ± 5

773

774

775 **Table 4**. Statistical analysis (difference factor, f_1; similarity factor, f_2) of the release

776 profiles for the buccal films. Similarity is indicated as accepted (+) or rejected (-).

Formulation	f_1	f_2	similarity
P1–P5	19.40	36.70	-
P1–P9	29.44	28.30	-
P5–P9	12.46	52.27	+

777

778

779   **Table 5.** Kinetics modeling of buccal films P1, P5, and P9.

Formulation	Higuchi		Korsmeyer–Peppas		
	k	R^2	k	n	R^2
P1	2.47	0.373	-	-	-
P5	5.96	0.861	-	-	-
P9	6.89	0.820	22.57	0.457	0.907

780

781

782 **Table 6**. Permeation parameters of buccal films across porcine buccal mucosa.

Formulation	J_{ss} [μg cm^{-2} h^{-1}]	$P_{app} \times 10^3$ [cm h^{-1}]	Lag time [h]	Extracted [mg]
P5	3.65 ± 0.35	4.82 ± 0.47	0.50 ± 0.06	77.4 ± 8.2
P9	11.50 ± 0.61	8.36 ± 0.78	0.78 ± 0.05	166.7 ± 15.6

783

784

785 **Figure 1**

HPMC
filament

FDM
printing

EtOH:PG
ink

IBU

HPMC
mucoadhesive
substrate

inkjet
printing
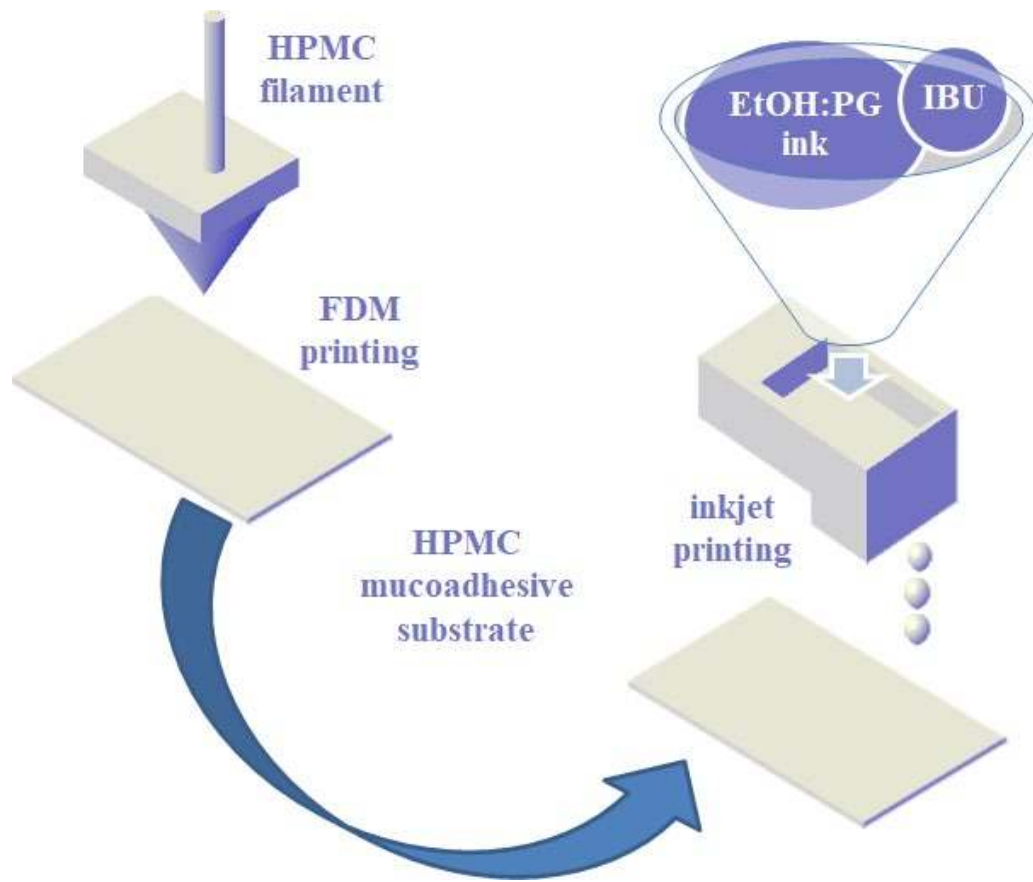
786

787

788   **Figure 2**

789

790
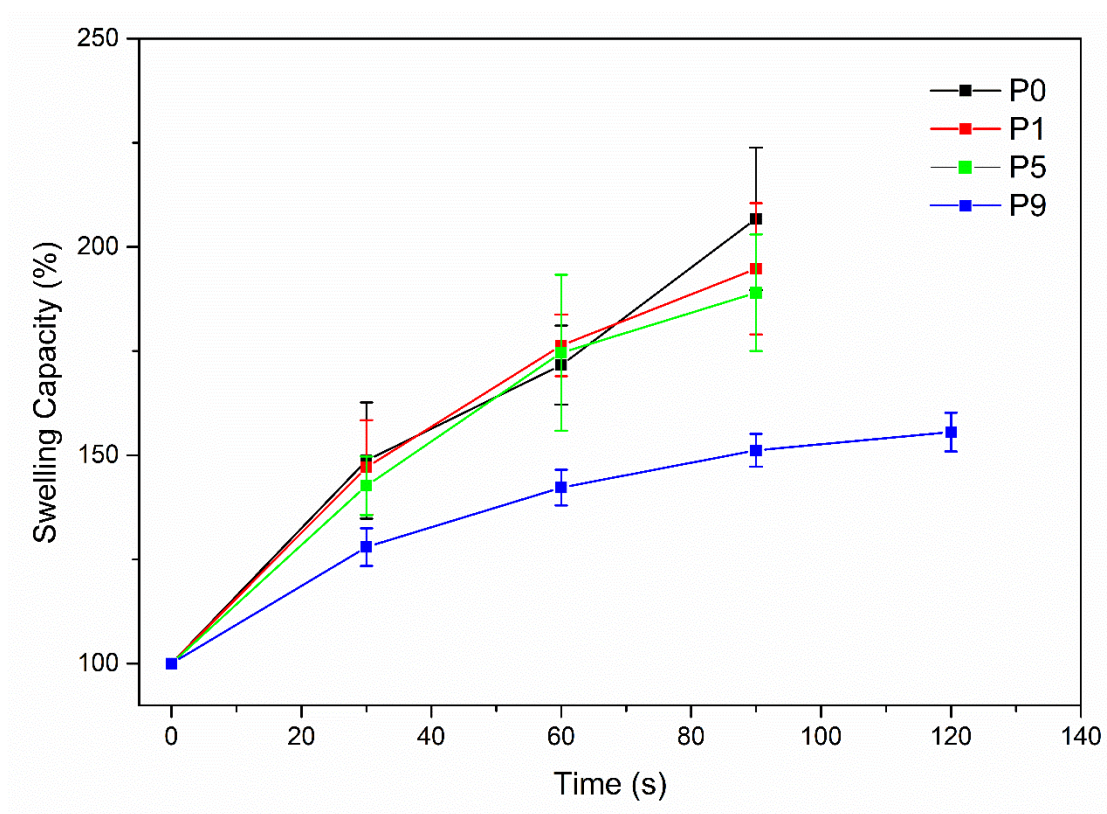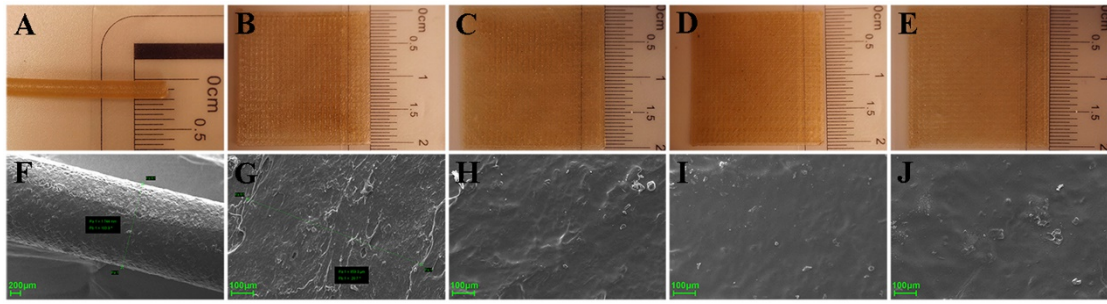
Figure 3

794 **Figure 4**
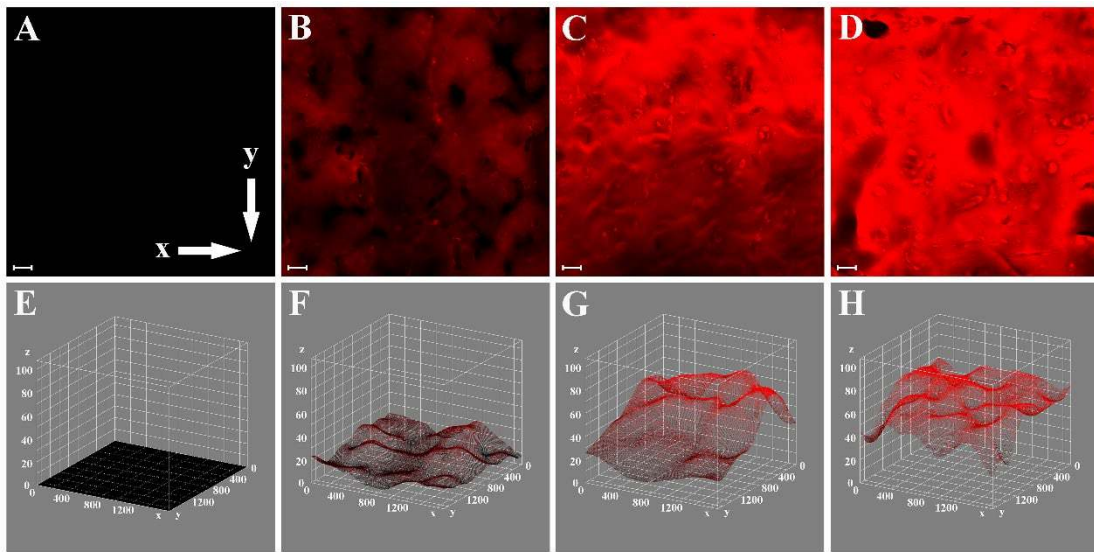
795

796

797   **Figure 5**
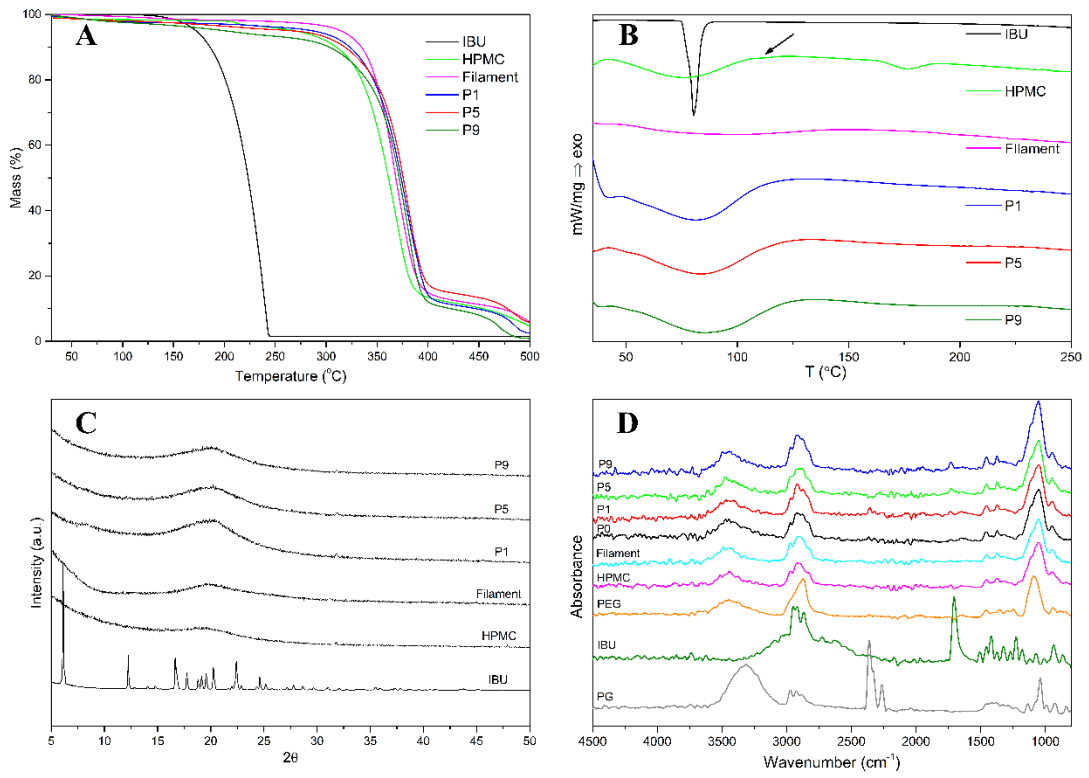
798

799
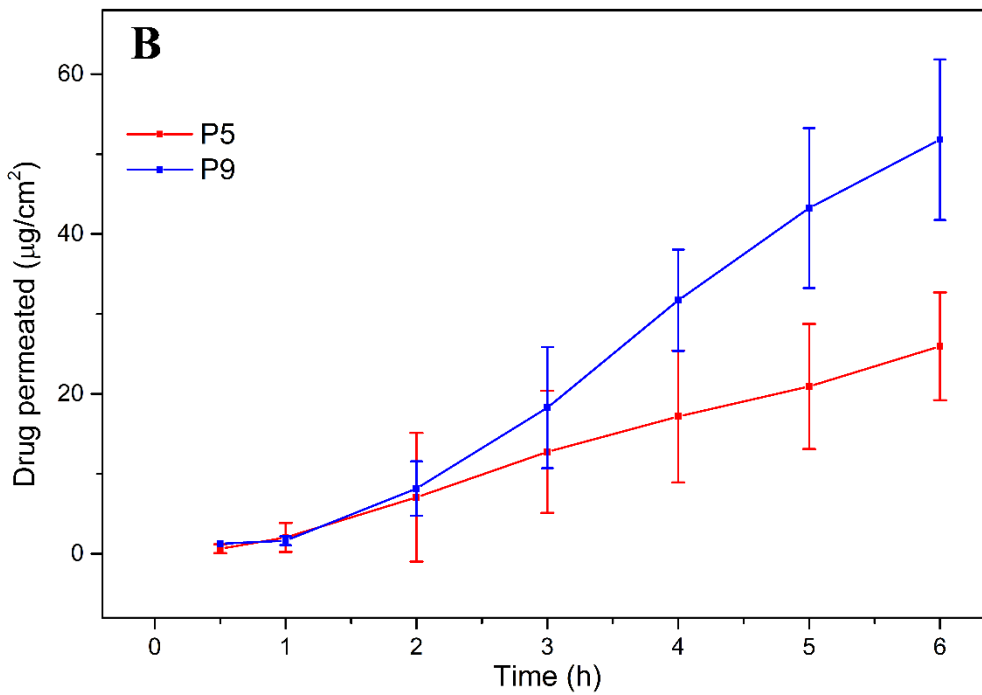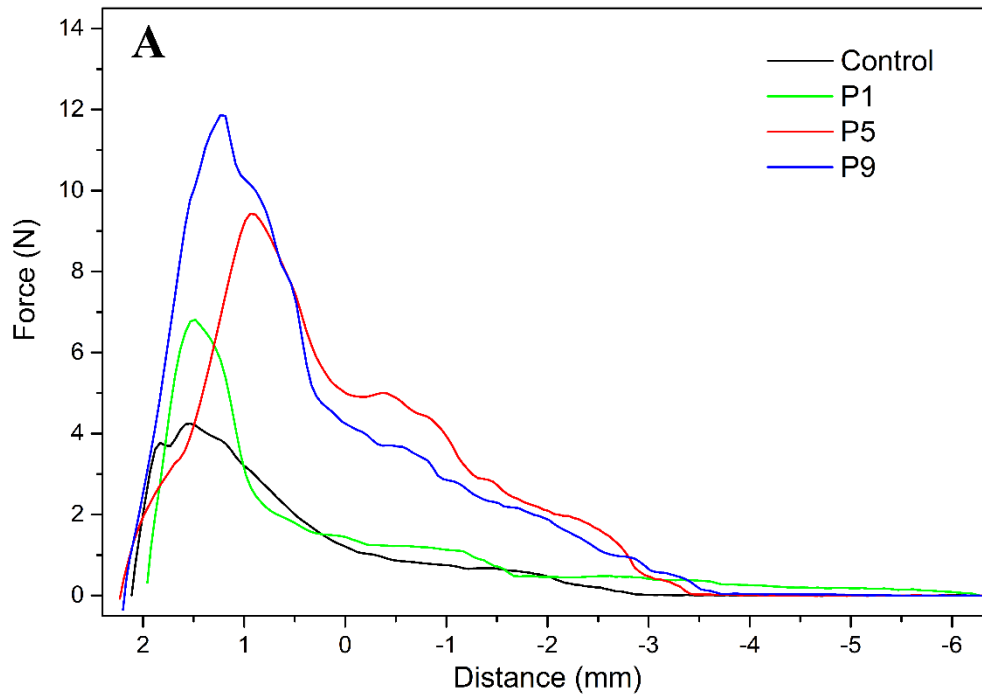
800   **Figure 6**
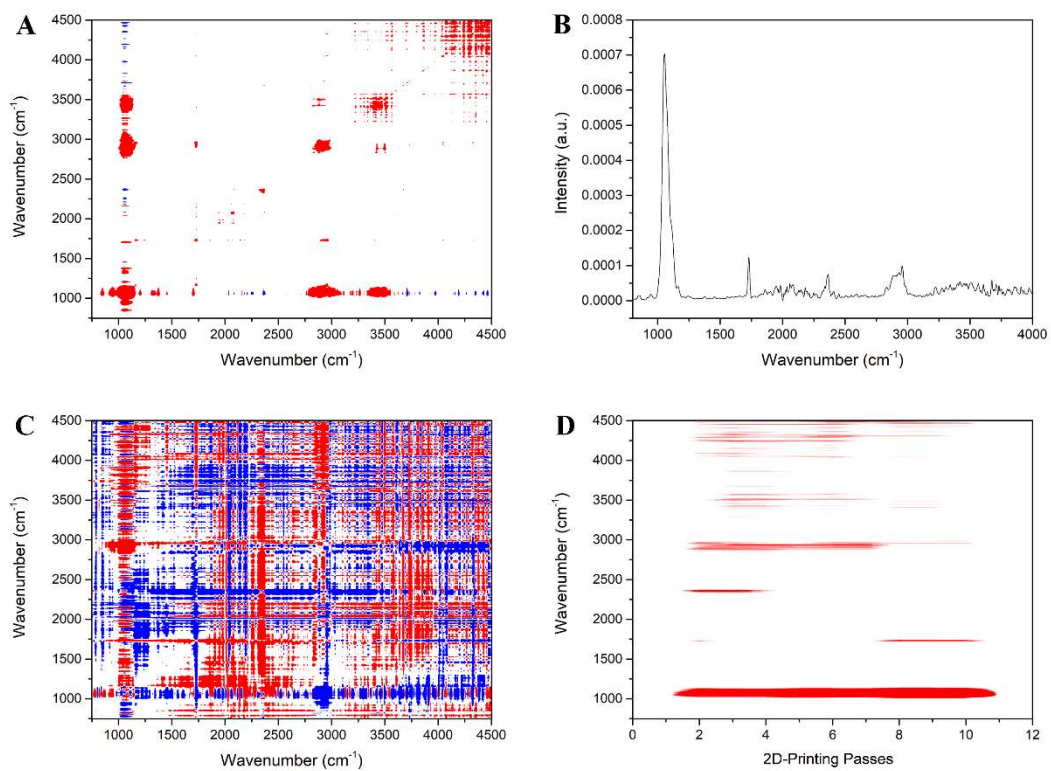
801
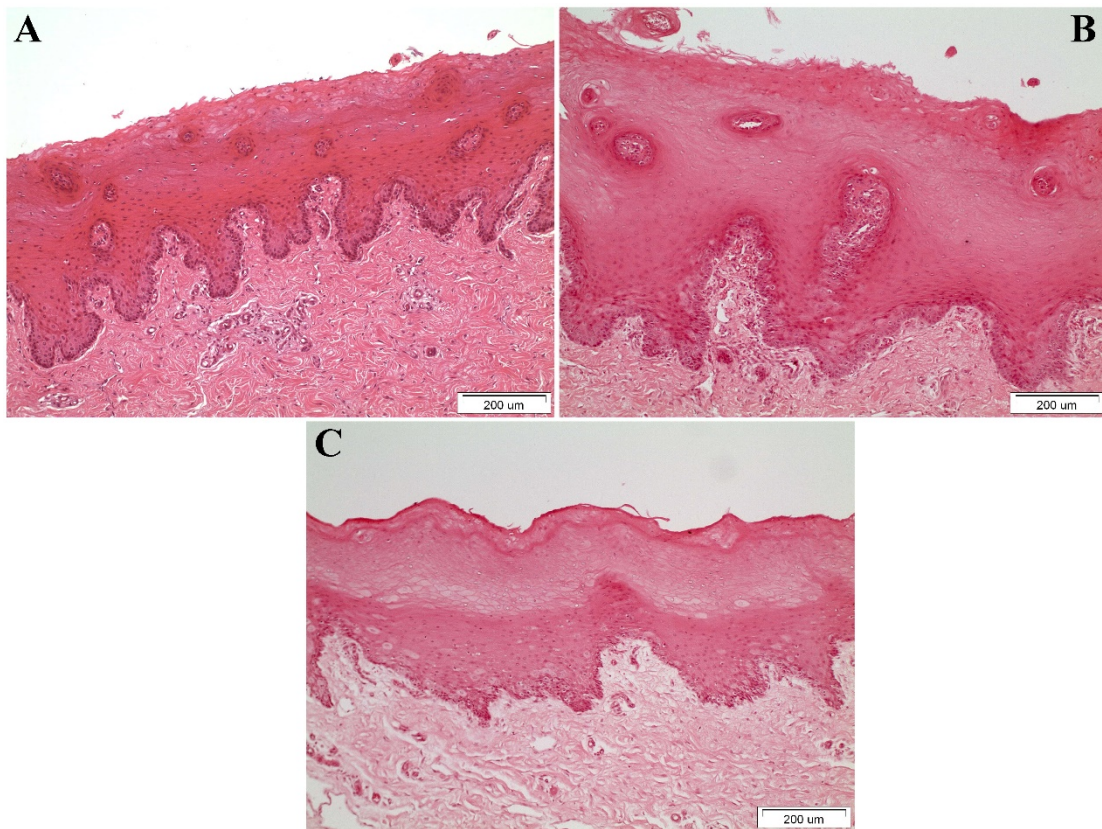
802

803   **Figure 7**
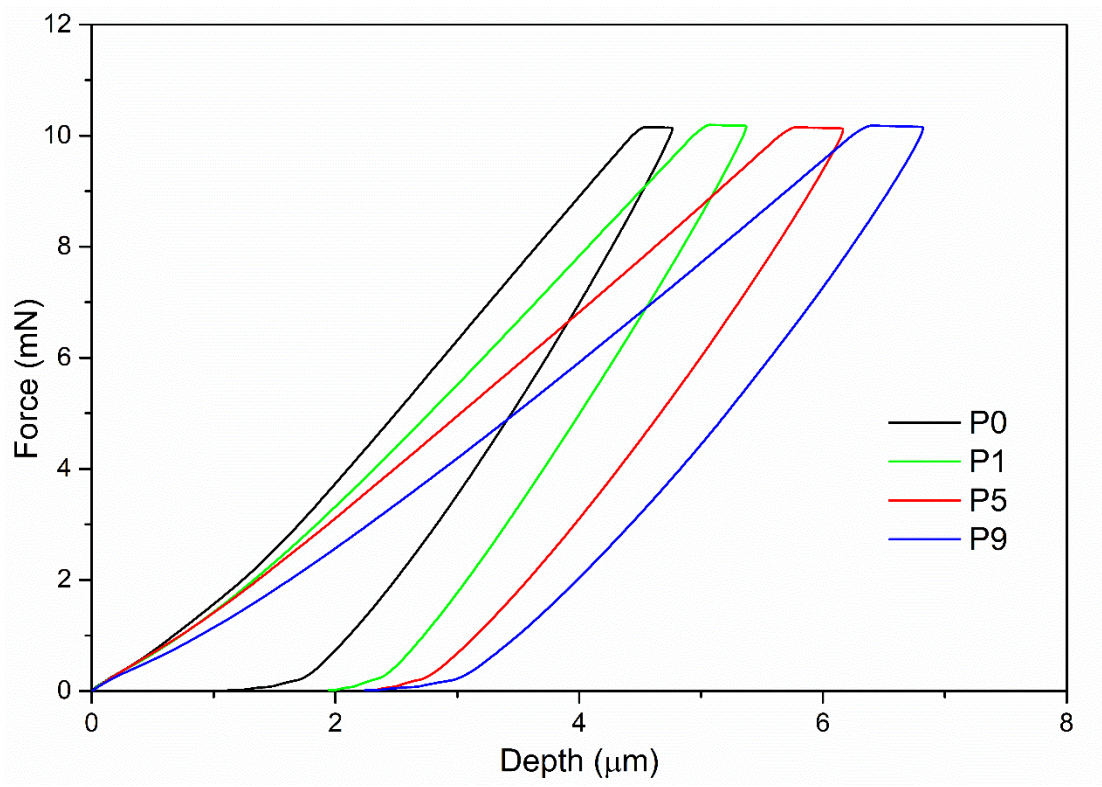
804

805

806 **Figure 8**

807

808
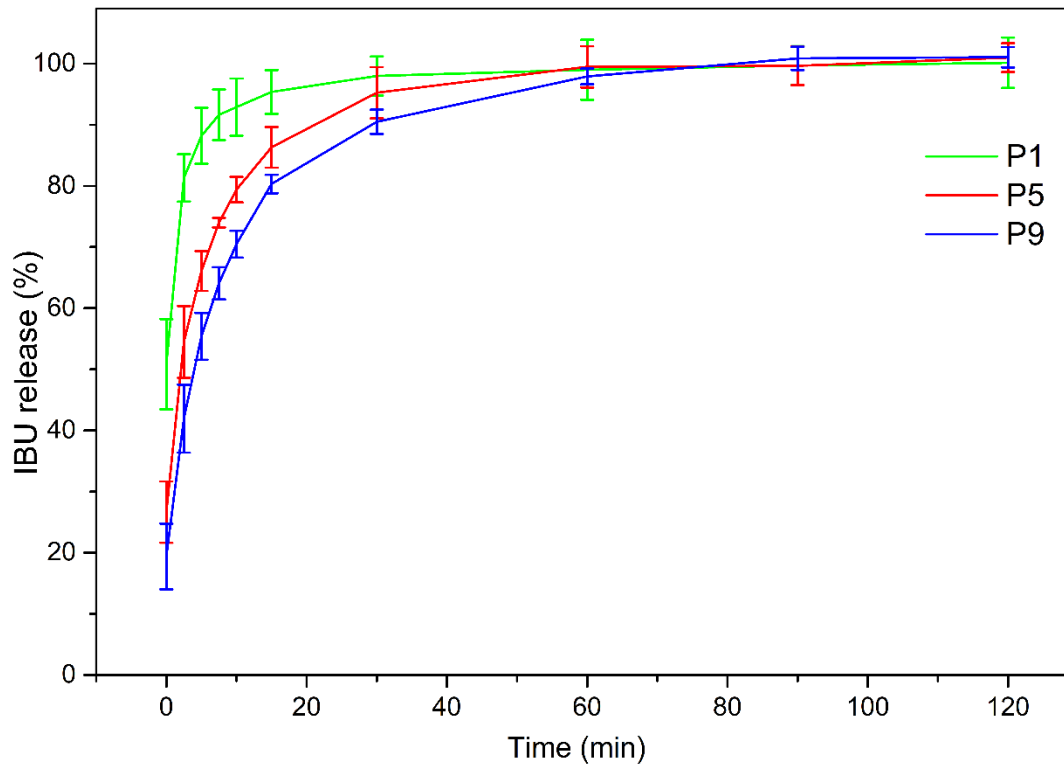
Figure 9

812   **Figure 10**

813

814

Figure Captions

Figure 1. The manufacturing approach followed in the current study, presenting the FDM-printing of mucoadhesive films, which serve as substrates for the inkjet deposition of a drug-containing liquid ink.

Figure 2. Hydration profiles of formulations with 0 (P0), 1 (P1), 5 (P5), and 9 (P9) IP passes.

Figure 3. Digital stereoscope images (A–E) and SEM images (F–J) of filaments and formulations with 0, 1, 5, and 9 IP passes (from left to right).

Figure 4. Confocal images (50-μm scale bar) and 3D surface plots of the fluorescence intensity (z-axis) across the x–y plane for formulations with 0 (A, E), 1 (B, F), 5 (C, G), and 9 (D, H) IP passes.

Figure 5. (A) TGA thermograms, (B) DSC thermograms, (C) XRPD spectra, and (D) FTIR spectra of the raw materials, filaments, and buccal films with 0 (P0), 1 (P1), 5 (P5), and 9 (P9) IP passes.

Figure 6. A) Synchronous contour plot, B) dynamic intensity changes (auto-peaks), C) asynchronous contour plot, and D) moving-window mapping of the effect of the external perturbation (number of IP passes, 0–12) on the spectral data of the formulations.

840   **Figure 7.** Typical force–depth profiles of the HPMC-based platforms P0, P1, P5, and

841   P9, obtained via indentation tests.

842

843   **Figure 8.** Release profiles of IBU from the P1, P5, and P9 buccal films.

844

845   **Figure 9.** (A) Mucoadhesion plot of force versus distance and (B) permeation profiles

846   of the buccal films.

847

848   **Figure 10.** Post-permeation images (200-μm scale bars) of porcine buccal mucosa for

849   formulations (A) P0, (B) P5, and (C) P9.

850